




8-1-2016

Single-Mode Optical Waveguides on Native High-Refractive-Index Substrates

Richard R. Grote
University of Pennsylvania

Lee C. Bassett
University of Pennsylvania, lbassett@seas.upenn.edu

Follow this and additional works at: http://repository.upenn.edu/ease_papers

 Part of the [Electromagnetics and Photonics Commons](#), [Optics Commons](#), and the [Semiconductor and Optical Materials Commons](#)

Recommended Citation

Richard R. Grote and Lee C. Bassett, "Single-Mode Optical Waveguides on Native High-Refractive-Index Substrates", *APL Photonics* 1. August 2016. <http://dx.doi.org/http://dx.doi.org/10.1063/1.4955065>

This paper is posted at ScholarlyCommons. http://repository.upenn.edu/ease_papers/751
For more information, please contact repository@pobox.upenn.edu.

Single-Mode Optical Waveguides on Native High-Refractive-Index Substrates

Abstract

High-refractive-index semiconductor optical waveguides form the basis for modern photonic integrated circuits (PICs). However, conventional methods for achieving optical confinement require a thick lower-refractive-index support layer that impedes large-scale co-integration with electronics and limits the materials on which PICs can be fabricated. To address this challenge, we present a general architecture for single-mode waveguides that confine light in a high-refractive-index material on a native substrate. The waveguide consists of a high-aspect-ratio fin of the guiding material surrounded by lower-refractive-index dielectrics and is compatible with standard top-down fabrication techniques. This letter describes a physically intuitive, semi-analytical, effective index model for designing fin waveguides, which is confirmed with fully vectorial numerical simulations. Design examples are presented for diamond and silicon at visible and telecommunications wavelengths, respectively, along with calculations of propagation loss due to bending, scattering, and substrate leakage. Potential methods of fabrication are also discussed. The proposed waveguide geometry allows PICs to be fabricated alongside silicon CMOS electronics on the same wafer, removes the need for heteroepitaxy in III-V PICs, and will enable wafer-scale photonic integration on emerging material platforms such as diamond and SiC.

Keywords

Waveguides, Diamond, Integrated Photonics

Disciplines

Electromagnetics and Photonics | Engineering | Optics | Semiconductor and Optical Materials

Single-mode optical waveguides on native high-refractive-index substrates

Richard R. Grote and Lee C. Bassett^a

Quantum Engineering Laboratory, Department of Electrical and Systems Engineering, University of Pennsylvania, 200 S. 33rd Street, Philadelphia, Pennsylvania 19104, USA

(Received 22 March 2016; accepted 20 June 2016; published online 1 August 2016)

High-refractive-index semiconductor optical waveguides form the basis for modern photonic integrated circuits (PICs). However, conventional methods for achieving optical confinement require a thick lower-refractive-index support layer that impedes large-scale co-integration with electronics and limits the materials on which PICs can be fabricated. To address this challenge, we present a general architecture for single-mode waveguides that confine light in a high-refractive-index material on a native substrate. The waveguide consists of a high-aspect-ratio fin of the guiding material surrounded by lower-refractive-index dielectrics and is compatible with standard top-down fabrication techniques. This letter describes a physically intuitive, semi-analytical, effective index model for designing fin waveguides, which is confirmed with fully vectorial numerical simulations. Design examples are presented for diamond and silicon at visible and telecommunications wavelengths, respectively, along with calculations of propagation loss due to bending, scattering, and substrate leakage. Potential methods of fabrication are also discussed. The proposed waveguide geometry allows PICs to be fabricated alongside silicon CMOS electronics on the same wafer, removes the need for heteroepitaxy in III-V PICs, and will enable wafer-scale photonic integration on emerging material platforms such as diamond and SiC. © 2016 Author(s). All article content, except where otherwise noted, is licensed under a Creative Commons Attribution (CC BY) license (<http://creativecommons.org/licenses/by/4.0/>). [<http://dx.doi.org/10.1063/1.4955065>]

Photonic integrated circuits (PICs) are rapidly being developed for high-refractive index materials that allow for tight optical confinement, small on-chip bend radii, and strong light-matter interactions. For example, high-performance PICs in both silicon¹ and InP^{2,3} platforms are playing an increasingly important role in data applications with the potential to enable exascale computing⁴ and on-chip core-to-core optical communication.⁵ Similarly, wide-band gap semiconductors, such as diamond^{6–13} and SiC,¹⁴ have emerged as promising materials for a plethora of new PIC applications. Among these are non-linear optics^{12–14} and integrated quantum information processing,^{8–11,15} which is enabled by the presence of spin defects with desirable quantum properties.^{16,17}

Common to all of these applications is a need for low-propagation-loss single-mode waveguides that can be fabricated on a high-refractive-index substrate in a scalable fashion. While a high refractive index is beneficial for optical design, it also requires a buried lower-refractive-index layer and the transfer or growth of thin films of high-index material,^{1–3,6–8,10,12–14,18} free-standing structures,^{9,11,19} or pedestals²⁰ to minimize optical power leakage from the waveguide into the substrate. These approaches limit the device robustness, uniformity, and scalability required for the development of dense PICs on wide-bandgap semiconductors.

Even on mature PIC platforms, optical confinement presents significant technological challenges. In silicon photonics, the buried-oxide-layer thickness required for optical confinement is much larger than the optimum for VLSI electronics, making co-integration difficult.^{5,18,19} For

^aAuthor to whom correspondence should be addressed. Electronic mail: lbassett@seas.upenn.edu



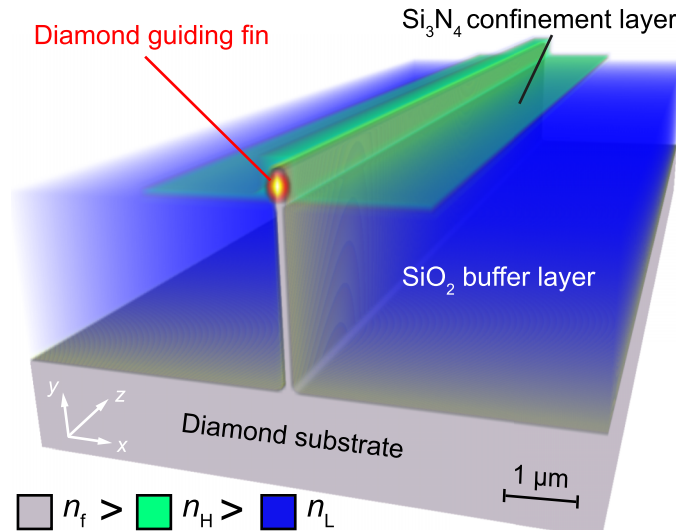


FIG. 1. The fin waveguide: An example of a fin waveguide on a diamond substrate designed for $\lambda = 637$ nm. The geometry supports a single mode when $n_f > n_H > n_L$. The profile of the confined optical mode shown in cross section has been calculated using finite difference method.

InP-based PICs, optical confinement is limited by the low index contrast between InP and InGaAsP.^{2,3}

Here, we propose a new type of waveguide optimized for high-index substrates that utilizes stacked dielectric layers to confine light in the top of a fin of high-index material. An example of a $\text{SiO}_2/\text{Si}_3\text{N}_4$ stack on a diamond fin/substrate at a wavelength of $\lambda = 637$ nm is shown in Fig. 1. Although the refractive index of both the buffer and confinement layers ($n_L = n_{\text{SiO}_2} \approx 1.45$ and $n_H = n_{\text{Si}_3\text{N}_4} \approx 2.0$, respectively) is lower than that of the fin and substrate ($n_f = n_{\text{diamond}} \approx 2.4$), the proposed design achieves confinement by engineering the *effective index*, resulting in an optical mode confined within the high-index material (diamond in the case of Fig. 1). This waveguide mode is a localized eigenmode that can propagate without leaking power into the underlying substrate, while the waveguide itself can be fabricated using conventional top-down lithography, etching, dielectric deposition, and planarization techniques. Though optical confinement has been achieved by effective index variations in many contexts, including high- Q cavities formed by photonic crystal waveguides²¹ and photonic crystal fibers,²² our application of this approach to vertically stacked slab waveguides obviates the need for a buried low-index layer, providing a pathway towards large-area, scalable PICs on native substrates.

Figures 2(a) and 2(b) illustrate an intuitive physical picture that accounts for optical confinement in the fin waveguide geometry using the effective index method,²³ the results of which are confirmed using a fully vectorial finite difference method.²⁴ By treating the two-dimensional cross section of the \hat{z} -invariant waveguide dielectric topology in Fig. 2(a) as two stacked slab waveguides with horizontal (\hat{x}) confinement, a slab waveguide with vertical (\hat{y}) confinement can be formed from the slab-waveguide effective indices in \hat{x} . In Fig. 2(b), the two slab waveguides comprised of $n_H/n_f/n_H$ (Slab 1) and $n_L/n_f/n_L$ (Slab 2) from Fig. 2(a) are replaced by homogeneous layers in \hat{x} with the effective indices of the lowest-order supported modes $n_{\text{eff},1}^x$ and $n_{\text{eff},2}^x$, respectively, where the effective index, $n_{\text{eff},i}^x = \beta_i^x/k_0$, is equal to the slab waveguide propagation constant in \hat{z} , β_i^x , of Slab i divided by the free space wavenumber, $k_0 = 2\pi/\lambda$. The dispersion curves of the two slabs as a function of the normalized waveguide width, w/λ , are shown in Fig. 2(c) with example refractive index values of $n_f = 2.5$, $n_H = 2.0$, and $n_L = 1.5$.

This treatment is a key to understanding the nature of confinement in the fin structure: a fin mode exists when the effective index of the two-dimensionally confined structure, n_{eff} , satisfies the condition: $n_{\text{eff},1}^x > n_{\text{eff}} > \max\{n_{\text{eff},2}^x, n_H\}$, as indicated by the green and blue shaded regions in Fig. 2(c). When this condition is not met, the confined modes are degenerate with a continuum

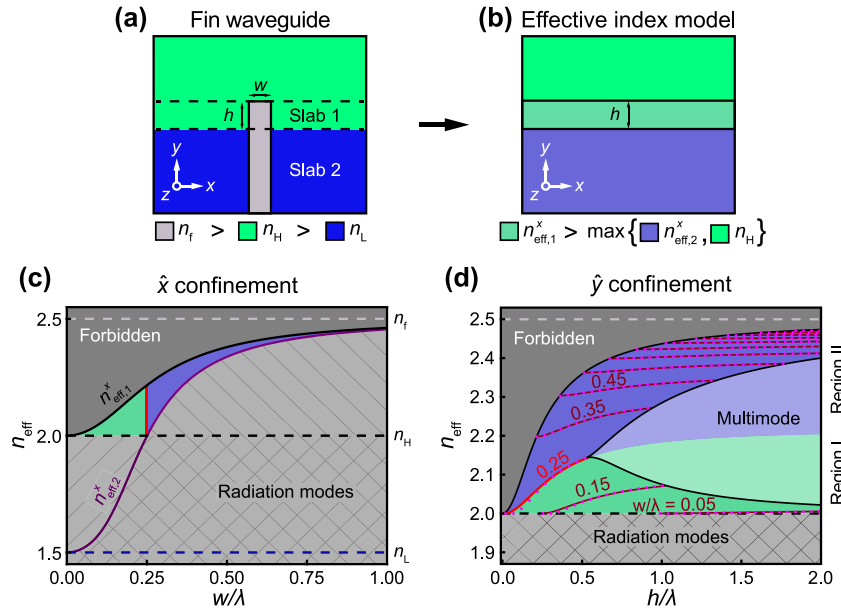


FIG. 2. Generalized fin waveguide dispersion: (a) Cross section of the fin waveguide geometry. Dashed lines mark regions that are approximated by effective indices in (b). (c) Dispersion of the fin waveguide as a function of w/λ . The region in which modes are confined (blue and green shading) is bound by the effective indices of the slab waveguides in (a). (d) Dispersion of the fin-waveguide as a function of h/λ . Semi-analytical curves are plotted for specific values of w/λ , and points are the result of fully vectorial finite difference method simulations.

of radiation modes and become leaky, as indicated by the gray hatched region in Fig. 2(c). In essence, vertical confinement of the fin waveguide mode is achieved by total internal reflection at the interface between slab waveguides rather than the interface between homogeneous media. As a consequence of the effective index confinement in the fin structure, only a single mode in \hat{x} is supported for the refractive index values chosen in Fig. 2(c). Higher-order modes can be confined for a different choice of material indices, but only if higher-order modes of Slab 1 are contained in the blue or green shaded region of Fig. 2(c), i.e., they must have an effective index larger than the lowest-order mode of Slab 2.

The supported modes of the two-dimensionally confined structure are found by solving for the modes of the \hat{y} -confined slab waveguide in Fig. 2(b). The resulting fin mode dispersion as a function of normalized waveguide height, h/λ [Fig. 2(d)], has two distinct regions that depend on the fin width, w ,

$$\text{Region I : } n_{\text{eff},2}^x < n_H; w < w_{\text{symm}} \text{ (green shading),}$$

$$\text{Region II : } n_{\text{eff},2}^x > n_H; w > w_{\text{symm}} \text{ (blue shading).}$$

The boundary between these two regions occurs when $n_{\text{eff},2}^x = n_H$ at a width that we label $w = w_{\text{symm}}$, which is indicated by a vertical red line in Fig. 2(c) and the red dispersion curve ($w_{\text{symm}}/\lambda = 0.25$) in Fig. 2(d). For an asymmetric slab waveguide, the higher-refractive-index cladding determines both the cutoff condition and the effective mode width. In **Region I**, the properties of the asymmetric waveguide are determined by n_H , while in **Region II**, this role is taken by $n_{\text{eff},2}^x$. The change in cutoff condition between the two regions causes the inflection point in the cutoff height [boundary for the multimode region in Fig. 2(d)] at w_{symm} . While the fin waveguide can only be single or few mode in width, it can be multimode in height, as indicated in Fig. 2(d).

The dispersion curves provide the allowable geometry and wavelength at which confined modes are supported. Within these constraints, the mode area, A_{eff} , and confinement factor, Γ , which quantifies the overlap between the optical mode and the guiding material, provide useful design metrics for maximizing light-matter interactions in fin waveguides.²⁵ In Fig 3(a), we calculate A_{eff} for a series of w/λ and plot the minimum, A_{min} , along with the corresponding height, h_{min}/λ . Mode

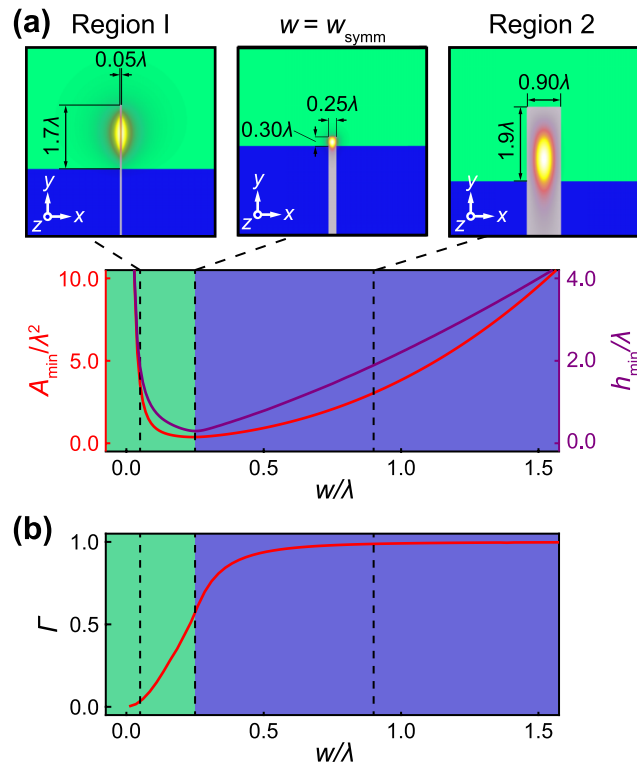


FIG. 3. Optical confinement of the fin waveguide: (a) Minimum mode area as a function of w/λ and the corresponding h_{\min}/λ . Mode profiles at the three values of w/λ marked by dashed lines are plotted above. The smallest achievable mode area occurs when $n_H = n_{\text{eff},2}^x$ at $w_{\text{symm}}/\lambda = 0.25$. (b) The confinement factor, Γ , measures the geometric overlap between the optical mode and the high-index material.

intensity profiles for three values of w/λ are also shown in Fig. 3(a), and the corresponding Γ at A_{\min} is plotted in Fig. 3(b).

In **Region I** most of the field penetration occurs in the confinement layer, relaxing the requirements on the buffer layer thickness for low leakage at the expense of reduced Γ . Conversely, in **Region II** A_{\min} increases with w/λ , Γ approaches unity, and the mode extends within the fin into the buffer layer. Waveguides designed in this region may be desirable for high-power applications. The tightest confinement (smallest A_{\min}) occurs at w_{symm} , which also corresponds to the maximum group index, $N_g = c/v_g$, where c is the vacuum speed of light and v_g is the modal group velocity, making $w = w_{\text{symm}}$ an ideal design criterion for maximizing light-matter interactions.²⁵ The waveguide properties in Figs. 2 and 3 have been calculated for the lowest-order mode with the dominant electric field component along \hat{x} , commonly referred to as the quasi-TE mode. Discussion of the lowest order quasi-TM mode (dominant electric field component along \hat{y}), higher order modes, and further details of our semi-analytical and numerical calculations are provided in the supplementary material.²⁵

To illustrate the potential of the fin waveguide, we explore geometries in two important material platforms for PICs: diamond and silicon. The diamond waveguide is designed with an SiO_2 buffer layer, a conformal 200 nm-thick Si_3N_4 confinement layer, and SiO_2 overcladding for single-mode operation at $\lambda = 637$ nm. The operating wavelength corresponds to the nitrogen-vacancy center zero phonon line,⁸ which is used to achieve coherent spin-light interactions²⁶ and distributed entanglement²⁷ between diamond spins. We design the waveguide for the tightest confinement with $w = w_{\text{symm}}$ as discussed above. The waveguide dispersion and group index are shown in Fig. 4(a), along with the waveguide dimensions and calculated mode intensity profile at $\lambda = 637$ nm. For a buffer layer thickness exceeding 1.0 μm (total fin height 1.35 μm , corresponding to an aspect ratio $>6.75:1$) the calculated propagation loss due to substrate leakage is <0.15 dB/cm, which is small

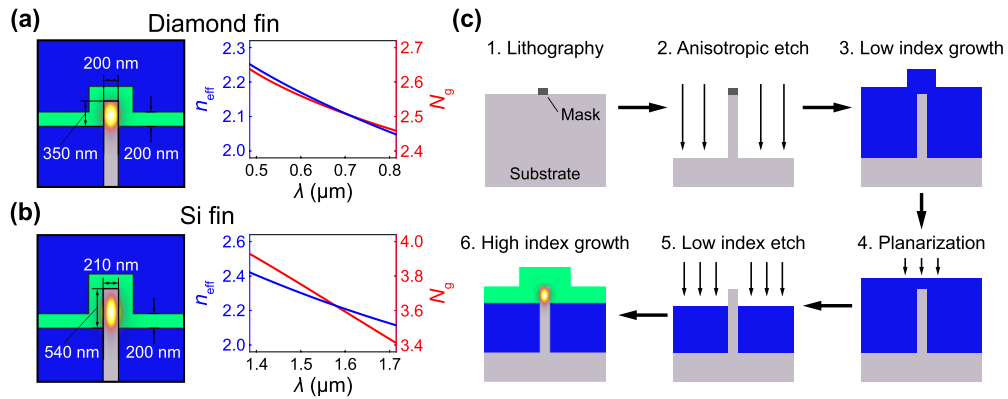


FIG. 4. Design examples: Fin waveguides designed for maximum confinement in (a) diamond at $\lambda = 637$ nm and (b) silicon at $\lambda = 1.55$ μm . (c) Fabrication process for a fin waveguide.

enough that scattering due to fabrication imperfections in a realistic device would be expected to dominate (see below). The bending loss for a radius of 10 μm is determined to be <0.03 dB per 90° bend with a buffer layer thickness of 1.0 μm , corresponding to an unloaded Q exceeding 60 000 for a 20 μm -diameter ring resonator.

Similarly, the silicon waveguide depicted in Fig. 4(b) is designed for minimum mode area at $\lambda = 1.55$ μm for telecommunications applications. With a buffer layer thickness exceeding 1.5 μm (fin aspect ratio $>9.75:1$), the propagation loss due to substrate leakage is calculated to be <0.1 dB/cm. The bending loss for a radius of 10 μm is determined to be <0.1 dB per 90° bend with a buffer layer of 1.5 μm , corresponding to an unloaded Q exceeding 10,000 for a 20 μm -diameter ring resonator.

The predictions above ignore scattering losses due to sidewall roughness, which is a consequence of the dry etching techniques commonly used to fabricate waveguides. In comparison to conventional silicon waveguides, we find that the maximal-confinement fin architecture exhibits similar propagation loss due to sidewall roughness compared to a 500 nm \times 250 nm channel waveguide clad with air or SiO_2 . Results of these calculations, additional details of fin waveguide modeling, and a design example for SiC are provided in the supplementary material.²⁵

Figure 4(c) depicts a process flow for fabricating fin waveguides on an arbitrary high-index substrate. All of the steps are well-established, top-down fabrication techniques that can be applied to a wide range of materials. The required aspect ratios of the fins in Figs. 4(a) and 4(b) can be achieved through anisotropic inductively coupled plasma reactive ion etching (ICP-RIE), for which aspect ratios exceeding 10:1 in diamond²⁸ and 50:1 in Si²⁹ have been demonstrated. High-aspect-ratio fins are already employed in InP-based PICs,³⁰ where the fin waveguide design can provide an alternative to the conventional InGaAsP guiding layer, leading to higher confinement and smaller mode area.

The dielectric stack can be fabricated using standard lithography, deposition, and planarization techniques [Fig. 4(c)], following a similar process flow to that used for high-aspect-ratio ($>10:1$) CMOS FinFETs.³¹ Indeed, all of the required steps are silicon-CMOS compatible, providing exciting opportunities for the realization of electronic-photonic co-integration and novel device structures. For example, high-speed active devices in CMOS-compatible silicon PICs could be achieved through alignment of the fin waveguide with vertical p - i - n junctions.³² Although the examples in Figs. 4(a) and 4(b) use a $\text{SiO}_2/\text{Si}_3\text{N}_4$ dielectric stack, the fin waveguide can be designed for any pair of materials with $n_H > n_L$. Further details about the fabrication methods, alternative dielectric materials, and CMOS-compatible implementations are provided in the supplementary material.²⁵

One challenge with the proposed architecture is the incorporation of devices that are typically multimode, such as Y-branches and grating couplers, since higher-order modes in \hat{x} are leaky. We envision a solution to this challenge in the form of supermode devices, where multimode propagation is achieved by coupled arrays of single-mode waveguides.

In summary, we have proposed a new waveguide design for native high-refractive-index substrates. This method is compatible with standard fabrication processes and alleviates the need for a buried low-index layer, providing a potential route for CMOS-compatible co-integration of silicon photonics with VLSI electronics. Furthermore, the geometry can be adapted for any high-index substrate material, which will lead to rapid development of PICs on emerging materials platforms for nonlinear photonics, quantum information processing, and sensing applications.

We thank F. Aflatouni, J. Driscoll, S. Mann, A. Exarhos, and D. Hopper for helpful discussions.

- ¹ *Silicon Photonics: The State of the Art*, edited by G. T. Reed (John Wiley & Sons, Chichester, UK, 2008).
- ² L. Coldren, S. C. Nicholes, L. Johansson, S. Ristic, R. S. Guzzon, E. J. Norberg, U. Krishnamachari *et al.*, *IEEE J. Lightwave Technol.* **29**, 554 (2011).
- ³ M. Smit, X. Leijtens, H. Ambrosius, E. Bente, J. van der Tol, B. Smalbrugge, T. de Vries, E.-J. Geluk, J. Bolk, R. van Veldhoven *et al.*, *Semicond. Sci. Technol.* **29**, 083001 (2014).
- ⁴ S. Rumley, D. Nikolova, R. Hendry, Q. Li, D. Calhoun, and K. Bergman, *IEEE J. Lightwave Technol.* **33**, 547 (2015).
- ⁵ L. C. Kimerling, D.-L. Kwong, and K. Wada, *MRS Bull.* **39**, 687 (2014).
- ⁶ I. Aharonovich, A. D. Greentree, and S. Praver, *Nat. Photonics* **5**, 397 (2011).
- ⁷ S. Castelletto, J. Harrison, L. Marseglia, A. Stanley-Clarke, B. Gibson, B. Fairchild, J. Hadden, Y. D. Ho, M. Hiscocks, K. Ganesan *et al.*, *New J. Phys.* **13**, 025020 (2011).
- ⁸ A. Faraon, P. E. Barclay, C. Santori, K.-M. C. Fu, and R. G. Beausoleil, *Nat. Photonics* **5**, 301 (2011).
- ⁹ M. J. Burek, Y. Chu, M. S. Liddy, P. Patel, J. Rochman, S. Meesala, W. Hong, Q. Quan, M. D. Lukin, and M. Lončar, *Nat. Commun.* **5**, 5718 (2014).
- ¹⁰ N. Thomas, R. J. Barbour, Y. Song, M. L. Lee, and K.-M. C. Fu, *Opt. Express* **22**, 13555 (2014).
- ¹¹ S. L. Mouradian, T. Schröder, C. B. Poitras, L. Li, J. Goldstein, E. H. Chen, J. Cardenas, M. L. Markham, D. J. Twitchen, M. Lipson, and D. Englund, *Phys. Rev. X* **5**, 031009 (2015).
- ¹² B. Hausmann, I. Bulu, V. Venkataraman, P. Deotare, and M. Lončar, *Nat. Photonics* **8**, 369 (2014).
- ¹³ P. Latawiec, V. Venkataraman, M. J. Burek, B. J. Hausmann, I. Bulu, and M. Lončar, *Optica* **2**, 924 (2015).
- ¹⁴ J. Cardenas, M. Yu, Y. Okawachi, C. B. Poitras, R. K. Lau, A. Dutt, A. L. Gaeta, and M. Lipson, *Opt. Lett.* **40**, 4138 (2015).
- ¹⁵ W. Gao, A. Imamoglu, H. Bernien, and R. Hanson, *Nat. Photonics* **9**, 363 (2015).
- ¹⁶ J. Weber, W. Koehl, J. Varley, A. Janotti, B. Buckley, C. Van de Walle, and D. D. Awschalom, *Proc. Natl. Acad. Sci. U. S. A.* **107**, 8513 (2010).
- ¹⁷ D. D. Awschalom, L. C. Bassett, A. S. Dzurak, E. L. Hu, and J. R. Petta, *Science* **339**, 1174 (2013).
- ¹⁸ C. Sun, M. Georgas, J. Orcutt, B. Moss, Y.-H. Chen, J. Shainline, M. Wade, K. Mehta, K. Nammari, E. Timurdogan *et al.*, *IEEE J. Solid-State Circuits* **50**, 828 (2015).
- ¹⁹ J. S. Orcutt, A. Khilo, C. W. Holzwarth, M. A. Popović, H. Li, J. Sun, T. Bonifield, R. Hollingsworth, F. X. Kärtner, H. I. Smith *et al.*, *Opt. Express* **19**, 2335 (2011).
- ²⁰ P. T. Lin, V. Singh, Y. Cai, L. C. Kimerling, and A. Agarwal, *Opt. Lett.* **38**, 1031 (2013).
- ²¹ B.-S. Song, S. Noda, T. Asano, and Y. Akahane, *Nat. Mater.* **4**, 207 (2005).
- ²² J. Knight, T. Birks, P. S. J. Russell, and J. De Sandro, *J. Opt. Soc. Am. A* **15**, 748 (1998).
- ²³ A. Yariv and P. Yeh, *Photonics: Optical Electronics in Modern Communications*, 6th ed. (Oxford University Press, New York, 2007).
- ²⁴ A. B. Fallahkhair, K. S. Li, and T. E. Murphy, *IEEE J. Lightwave Technol.* **26**, 1423 (2008).
- ²⁵ See supplementary material at <http://dx.doi.org/10.1063/1.4955065> for additional details on the model and loss calculations.
- ²⁶ B. B. Buckley, G. D. Fuchs, L. C. Bassett, and D. D. Awschalom, *Science* **330**, 1212 (2010).
- ²⁷ H. Bernien, B. Hensen, W. Pfaff, G. Koolstra, M. Blok, L. Robledo, T. Tamirniau, M. Markham, D. Twitchen, L. Childress *et al.*, *Nature* **497**, 86 (2013).
- ²⁸ B. J. Hausmann, M. Khan, Y. Zhang, T. M. Babinec, K. Martinick, M. McCutcheon, P. R. Hemmer, and M. Lončar, *Diamond Relat. Mater.* **19**, 621 (2010).
- ²⁹ B. Wu, A. Kumar, and S. Pamarthy, *J. Appl. Phys.* **108**, 051101 (2010).
- ³⁰ S. Park, S.-S. Kim, L. Wang, and S.-T. Ho, *IEEE J. Quantum Electron.* **41**, 351 (2005).
- ³¹ C. Wu, D. Lin, A. Keshavarzi, C. Huang, C. Chan, C. Tseng, C. Chen, C. Hsieh, K. Wong, M. Cheng *et al.*, *2010 IEEE International Electron Devices Meeting (IEDM)* (IEEE, 2010), pp. 27–28.
- ³² A. Liu, L. Liao, D. Rubin, H. Nguyen, B. Ciftcioglu, Y. Chetrit, N. Izhaky, and M. Paniccia, *Opt. Express* **15**, 660 (2007).

Supplementary Material for: Single-Mode Optical Waveguides on Native High-Refractive-Index Substrates

Richard R. Grote and Lee C. Bassett*

*Quantum Engineering Laboratory, Department of Electrical and Systems Engineering,
University of Pennsylvania, 200 S. 33rd Street, Philadelphia, PA 19104, USA*

(Dated: June 14, 2016)

Details of the approximate and numerical methods used for analyzing the fin waveguide structure are provided, along with additional calculations of substrate leakage loss, bending loss, and scattering loss. A proposed fabrication flow is provided.

1. WAVEGUIDE DISPERSION DERIVATION AND DEFINITIONS

The supported modes of the \hat{z} -invariant refractive index profile, $n(x, y)$, in Fig. 2a of the main text can be solved by casting Maxwell's equations as an eigenvalue problem:

$$\hat{A}|m\rangle = \beta_m^2 |m\rangle \quad (\text{S.1})$$

where $\beta_m = k_0 n_{\text{eff}}^m$ is the propagation constant of mode m , $k_0 = \frac{2\pi}{\lambda}$ is the free space wavenumber, n_{eff}^m is the effective refractive index of mode m and the operator \hat{A} takes the following form when projected onto the position basis:

$$\hat{A} = \nabla_t^2 + k_0^2 n^2(x, y). \quad (\text{S.2})$$

The eigenvectors represent the transverse electric fields:

$$\hat{A}|\mathbf{E}_t^m\rangle = \beta_m^2 |\mathbf{E}_t^m\rangle \quad (\text{S.3})$$

where

$$|\mathbf{E}_t^m\rangle = \begin{bmatrix} E_x^m \\ E_y^m \end{bmatrix}. \quad (\text{S.4})$$

With two-dimensional confinement the two transverse field components are mixed by boundary conditions for the tangential electric fields and perpendicular displacement fields at the dielectric interfaces contained in $n^2(x, y)$. The modes of the two-dimensionally confined structure cannot be calculated analytically; however, solutions to equations (S.3) can be found using numerical approaches such as finite-difference method (FDM) [1]. An alternate approach is to use the effective index method [2, 3] to find an approximate solution by treating equation (S.1) as two separable problems in \hat{x} and \hat{y} . We use the effective index method outlined in the following section to find approximate solutions to the fin waveguide dispersion, and verify our calculations with FDM [1].

A. Effective index method

In the one-dimensional analysis for \hat{x} , $n^2(x, y) \rightarrow n_i^2(x)$, $\hat{A} \rightarrow \hat{A}_x = \frac{\partial^2}{\partial x^2} + k_0^2 n_i^2(x)$, and equation (S.3) reduces to two separable equations representing two orthogonal polarizations. We represent these polarizations by $r = \hat{x}$ for the horizontal (E_x)-polarization, and $r = \hat{y}$ for the vertical (E_y)-polarization. We follow the approach of [2] to solve for the slab waveguide effective indices. The indices of the \hat{x} confined slab waveguides shown in Fig. 2a of the main text are:

$$\text{Slab 1: } n_1(x) = \begin{cases} n_{c,1} = n_H, & x > \frac{w}{2} \\ n_f, & \frac{w}{2} > x > -\frac{w}{2} \\ n_{c,1} = n_H, & -\frac{w}{2} > x \end{cases} \quad (\text{S.5})$$

$$\text{Slab 2: } n_2(x) = \begin{cases} n_{c,2} = n_L, & x > \frac{w}{2} \\ n_f, & \frac{w}{2} > x > -\frac{w}{2} \\ n_{c,2} = n_L, & -\frac{w}{2} > x \end{cases} \quad (\text{S.6})$$

The field is assumed to be sinusoidal in the guiding region, and exponentially decaying outside. The phase constants for the field in each region are defined as:

$$\gamma_{c,i}^x = k_0 \sqrt{(n_{\text{eff},i}^x)^2 - n_{c,i}^2} \quad \text{cladding} \quad (\text{S.7})$$

$$k_{f,i}^x = k_0 \sqrt{n_f^2 - (n_{\text{eff},i}^x)^2} \quad \text{guiding region} \quad (\text{S.8})$$

where $i = 1, 2$, corresponding to Slab 1 and Slab 2, respectively. The effective index of Slab i , $n_{\text{eff},i}^x$, is found by matching the phase constants at the boundaries to find the following eigenvalue equations:

$$k_{x,i} w = (p_i + 1)\pi - 2 \tan^{-1} \left(\frac{k_{x,i}}{\gamma_{c,i}^x} \right), \quad r = \hat{y} \quad (\text{S.9})$$

$$k_{x,i} w = (p_i + 1)\pi - 2 \tan^{-1} \left(\frac{n_{c,i}}{n_f} \right)^2 \left(\frac{k_{x,i}}{\gamma_{c,i}^x} \right), \quad r = \hat{x} \quad (\text{S.10})$$

where $p_i = 0, 1, 2, \dots$ is the mode index for Slab i . The phase constants are related to β by equations (S.7) and

* Corresponding author: lbassett@seas.upenn.edu

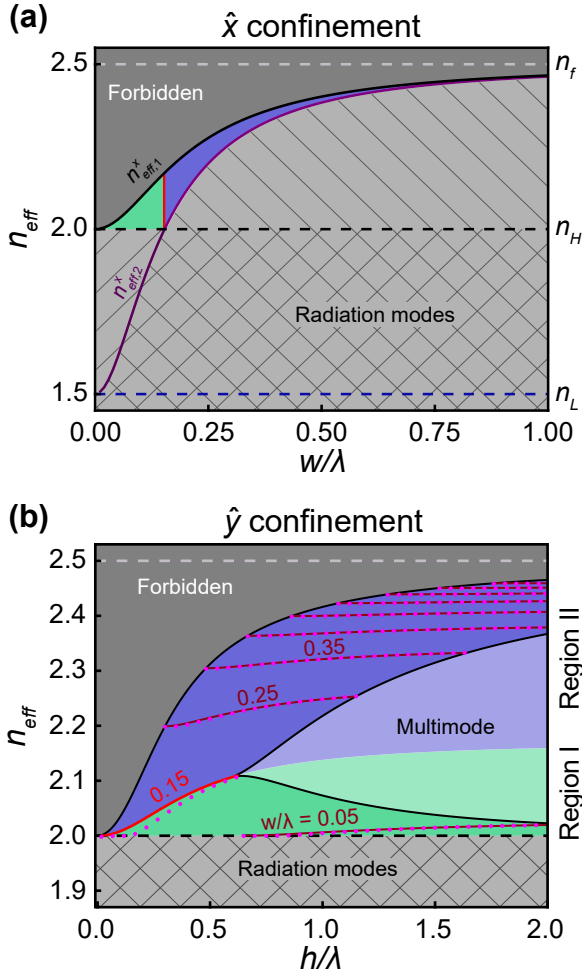


FIG. S1. Generalized fin waveguide dispersion for the lowest-order $|0, 0, \hat{y}\rangle$ (lowest order quasi-TM) mode. The waveguide geometry is shown in Fig. 2a of the main text.

(S.8), and solutions to the transcendental equations (S.9) or (S.10) provide the propagation constant for mode p_i . The cut-off condition for mode p_i can be expressed in terms of a minimum waveguide width:

$$w_{\text{cut-off}, p_i} = \frac{\lambda \pi p_i}{2\sqrt{n_f^2 - n_H^2}}, \quad p_i = 0, 1, 2, \dots \quad (\text{S.11})$$

Since the slab waveguides in \hat{x} are symmetric, there is no cut-off for the lowest order mode. Using the solutions for the slab waveguides in Fig. 2a of the main text, a \hat{y} -confined asymmetric slab waveguide (Fig. 2b of the main text) can be constructed with the following indices:

$$n(y) = \begin{cases} n_H, & y > \frac{h}{2} \\ n_{\text{eff},1}^x, & \frac{h}{2} > y > -\frac{h}{2} \\ n_{\text{eff},2}^x, & -\frac{h}{2} > y \end{cases} \quad (\text{S.12})$$

Using the nomenclature from [2], the asymmetric waveguide can be parameterized by a “substrate” with

refractive index n_s and “cladding” with refractive index n_c , where $n_f > n_s > n_c$. The effective index of Slab 2, $n_{\text{eff},2}^x$, depends on w/λ , thus we define the “substrate” and “cladding” indices in the following way:

$$n_s^y = \max \{ n_{\text{eff},2}^x, n_H \} \quad (\text{S.13})$$

$$n_c^y = \min \{ n_{\text{eff},2}^x, n_H \} \quad (\text{S.14})$$

With these definitions, the phase constants of the asymmetric waveguide are defined as follows:

$$\gamma_c^y = k_0 \sqrt{(n_{\text{eff}}^y)^2 - (n_c^y)^2} \quad (\text{S.15})$$

$$\gamma_s^y = k_0 \sqrt{(n_{\text{eff}}^y)^2 - (n_s^y)^2} \quad (\text{S.16})$$

$$k_y = k_0 \sqrt{(n_{\text{eff},1}^x)^2 - (n_{\text{eff}}^y)^2} \quad (\text{S.17})$$

which result in the following eigenvalue equations:

$$k_f^y h = (q+1)\pi - \tan^{-1} \left(\frac{k_f^y}{\gamma_s^y} \right) - \tan^{-1} \left(\frac{k_f^y}{\gamma_c^y} \right), \quad r = \hat{x} \quad (\text{S.18})$$

$$k_f^y h = (q+1)\pi - \tan^{-1} \left(\frac{n_s^y}{n_{\text{eff},1}^x} \right)^2 \left(\frac{k_f^y}{\gamma_s^y} \right) - \tan^{-1} \left(\frac{n_c^y}{n_{\text{eff},1}^x} \right)^2 \left(\frac{k_f^y}{\gamma_c^y} \right), \quad r = \hat{y} \quad (\text{S.19})$$

where $q = 0, 1, 2, \dots$ is the mode index for \hat{y} -confinement. The limits on allowable height for single mode operation are found by the cut-off condition for the lowest and first order modes of the asymmetric waveguide in Fig. S4d, which define the asymmetry parameter a^y :

$$a^y = \begin{cases} \frac{(n_s^y)^2 - (n_c^y)^2}{(n_{\text{eff},1}^x)^2 - (n_s^y)^2}, & r = \hat{x} \\ \left(\frac{n_{\text{eff},1}^x}{n_c^y} \right)^4 \frac{(n_s^y)^2 - (n_c^y)^2}{(n_{\text{eff},1}^x)^2 - (n_s^y)^2}, & r = \hat{y} \end{cases} \quad (\text{S.20})$$

The cut-off for mode $|0, q, r\rangle$ occurs at a height of:

$$h_{\text{cut-off}, q} = \frac{\lambda (\tan^{-1} \sqrt{a^y} + q\pi)}{2\pi \sqrt{(n_{\text{eff},1}^x)^2 - (n_s^y)^2}}, \quad q = 0, 1, 2, \dots \quad (\text{S.21})$$

Although pure polarization state solutions of the two-dimensionally confined modes do not exist, we use the mode numbers of the approximate effective index method solutions as waveguide eigenvalue labels:

$$|m\rangle \approx |p, q, r\rangle. \quad (\text{S.22})$$

All of the calculations in the main text have been performed for the $|0, 0, \hat{x}\rangle$ (lowest order quasi-TE) mode. The dispersion curves for the $|0, 0, \hat{y}\rangle$ (lowest order quasi-TM) mode of the structure in Fig. 2a of the main text are shown in Fig. S1.

In the example considered in Fig. 2 of the main text, the fin waveguide only supports a single horizontal mode ($p = 0$). For a different choice of n_L and n_H , such that the cut-off width of higher-order modes in the guiding layer is smaller than w_{symm} , additional horizontal modes can be supported, but the $p = 0$ mode for the buffer region always provides a lower limit for n_{eff} of confined modes as shown in Fig. 2c of the main text.

B. Power flow

The complex Poynting vector is defined as [4]:

$$S = -\frac{1}{2}\mathbf{E} \times \mathbf{H}^*. \quad (\text{S.23})$$

The \hat{z} -component of the Poynting vector represents the mode intensity profiles plotted in the main text and is defined as: $\text{Re}\{S_z\} = \text{Re}\{S \cdot \hat{z}\}$. The time-averaged power flow in \hat{z} can also be found from the complex Poynting vector:

$$P_z = \int \text{Re}\{S_z\} dA \quad (\text{S.24})$$

where A is area. For all calculations the modes are normalized such that $P_z = 1$ W.

For substrate loss calculations, there is power flow in \hat{y} , which is visualized by the \hat{y} -component of the Poynting vector, $\text{Re}\{S_y\} = \text{Re}\{S \cdot \hat{y}\}$, plotted in the insets of Fig. S3. The time-averaged power flow in \hat{y} is defined in a similar manner to equation (S.24).

C. Mode area and confinement factor

For small perturbations the effect of waveguiding on light-matter interaction can be approximated as [5, 6]:

$$\Delta n_{\text{eff}} \approx -\frac{\Delta n}{n} N_g F \quad (\text{S.25})$$

where Δn_{eff} is the change in the waveguide effective index due to a perturbation Δn , which depends on both the group index, N_g , and the fraction of mode energy contained in the perturbed region, F . The perturbation can be complex valued and can represent light-matter interactions such as absorption, gain, or material nonlinearity. Since we are concerned with perturbations to the waveguide core, F can be approximated by the confinement factor, Γ , which is defined as:

$$\Gamma = \frac{\int_{n_f} \text{Re}\{S_z\} dA}{\int \text{Re}\{S_z\} dA} \quad (\text{S.26})$$

and is plotted in Fig. 3b of the main text.

The ratio of the group velocity, v_g , to phase velocity, v_p , can be related to electric and magnetic field energies in the following way [7]:

$$\frac{v_g}{v_p} = F_t - F_z \quad (\text{S.27})$$

where F_t is the fraction of mode energy contained in the transverse fields, E_x, E_y, H_x, H_y , and F_z is the fraction of mode energy contained in the longitudinal fields, E_z, H_z . As was noted in [8], N_g is inversely proportional to the effective mode area, A_{eff} , as related through the energy contained in the longitudinal fields. Thus, A_{eff} can be used as a proxy for N_g , and the minimum mode area, A_{min} , corresponds to the maximum N_g .

The effective mode area, A_{eff} , plotted in Fig. 3a of the main text has been calculated as the area of an ellipse with axes defined by the modal effective width, w_{eff} and effective height, h_{eff} , as follows:

$$A_{\text{eff}} = \frac{\pi}{4} w_{\text{eff}} h_{\text{eff}} \quad (\text{S.28})$$

where w_{eff} and h_{eff} are calculated using the definitions in section 1:

$$w_{\text{eff}} = w + \frac{2}{\gamma_{c,1}^x} \quad (\text{S.29})$$

$$h_{\text{eff}} = h + \frac{1}{\gamma_s^y} + \frac{1}{\gamma_c^y} \quad (\text{S.30})$$

2. FIN WAVEGUIDE DESIGNS FOR SPECIFIC MATERIALS SYSTEMS

A. Silicon carbide design

A design for a silicon carbide fin waveguide with an SiO_2 buffer layer, a conformal 200 nm-thick Si_3N_4 confinement layer, and SiO_2 overcladding is shown in Fig. S2. Silicon carbide has recently emerged as a promising material for integrated non-linear photonics [9]. We note that this design is for cubic silicon carbide [12] with an isotropic refractive index; however, the fin waveguide geometry can also be applied to birefringent silicon carbide polytypes.

B. Substrate leakage

The substrate leakage as a function of buffer layer thickness shown in Fig. S3 has been calculated using

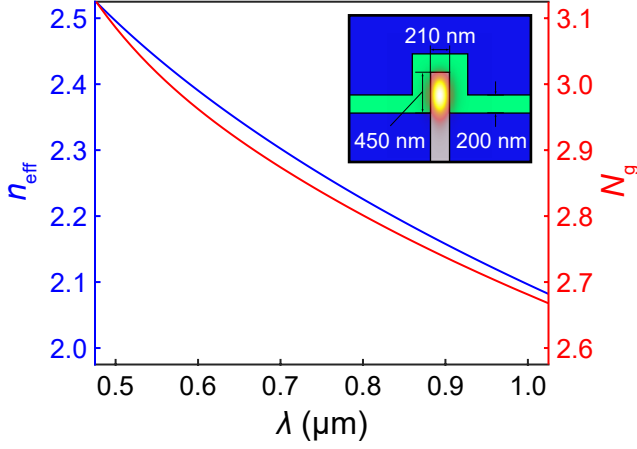


FIG. S2. **SiC design example.** Fin waveguide designed with SiC for visible and near-infrared wavelengths.

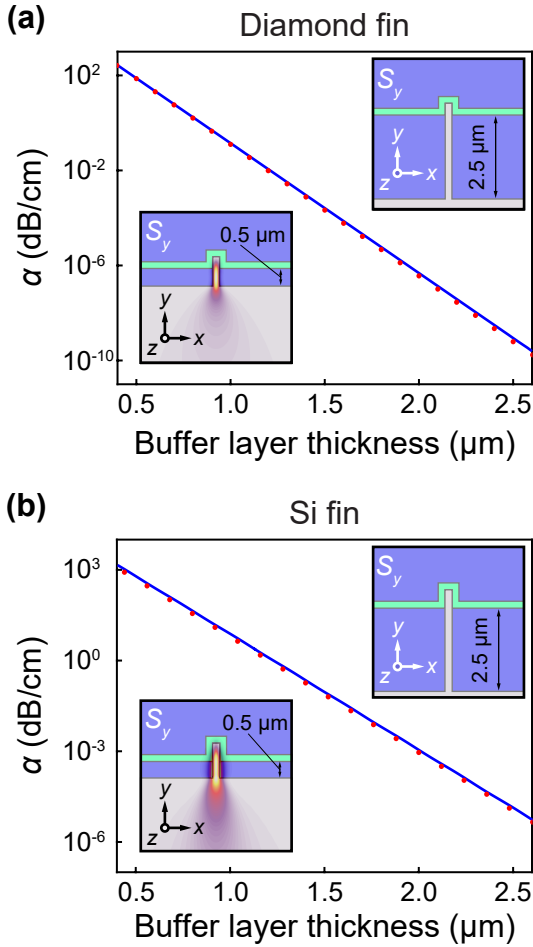


FIG. S3. **Substrate leakage.** The propagation loss, α , versus buffer layer thickness at the design wavelength is shown for (a) diamond fin, and (b) silicon fin. Solid lines and points represent two different calculation methods: absorbing boundary conditions (blue line) and coupled-mode theory (red points). (inset) Poynting vector in the y -direction, $\text{Re}\{S_y\}$, for buffer layer thicknesses of 0.5 μm and 2.5 μm .

two different methods: coupled-mode theory (red points) and absorbing boundary conditions (blue line). For the coupled-mode theory calculations the unperturbed mode is calculated using FDM without the high index substrate. Coupling of the unperturbed mode to the substrate is then calculated by using the following overlap integral [2, 3]:

$$\alpha_{\text{eff}} = \langle \mathbf{E} | \Delta \epsilon | \mathbf{E} \rangle = \frac{\omega \epsilon_0}{4} \int \mathbf{E}^* \cdot \Delta n^2(x, y) \mathbf{E} \, dA \quad (\text{S.31})$$

where $\Delta n^2(x, y) = n_f^2$ and the overlap region extends from the bottom of the buffer layer to $-\infty$ in \hat{y} , and from $-\infty$ to $+\infty$ in \hat{x} .

For the second method, the high-index substrate is included in the FDM calculation, and perfectly matched layer (PML) boundary conditions are added to the simulation cell. These boundary conditions allow for absorption at the simulation cell edge with minimal reflections. The FDM solver can find complex eigenvalues [1], which can be related to the propagation loss in the following manner:

$$\alpha_{\text{eff}} = \frac{4\pi \text{Im}\{n_{\text{eff}}\}}{\lambda} \quad (\text{S.32})$$

C. Bending loss

Bending loss of the structures in Fig. S4 is calculated in cylindrical coordinates with FDM using the method in [10], where the loss per 90° bend as a function of bend radius is shown. A buffer layer thickness of $t_B = 2.5 \mu\text{m}$ has been used for both waveguides. The bending-loss limited Q -factor of a ring resonator is also shown in Fig. S4, where $Q = \omega/\gamma$, $\omega = ck_0$ is the center frequency and $\gamma = \frac{\alpha_{\text{eff}} c}{N_g}$. The values in Fig. S4a,b are calculated at $\lambda = 637 \text{ nm}$ and $\lambda = 1.55 \mu\text{m}$, respectively.

D. Material dispersion models

The calculations in the main text use Sellmeier equations to model the various material refractive indices. The parameters for each material are given in table S1 and are used in the following equation [4]:

$$n^2 = 1 + \sum_i \frac{A_i \lambda^2}{\lambda^2 - \lambda_i^2} \quad (\text{S.33})$$

For the designs in Fig. 4 of the main text, the diamond material stack has the following refractive indices at 637 nm: $n_{\text{diamond}} = 2.41$, $n_{\text{Si}_3\text{N}_4} = 2.01$, and $n_{\text{SiO}_2} = 1.46$ as determined from Sellmeier equations for each material. The silicon material stack has the following refractive indices at $\lambda = 1.55 \mu\text{m}$: $n_{\text{Si}} = 3.48$, $n_{\text{Si}_3\text{N}_4} = 1.98$, and $n_{\text{SiO}_2} = 1.44$.

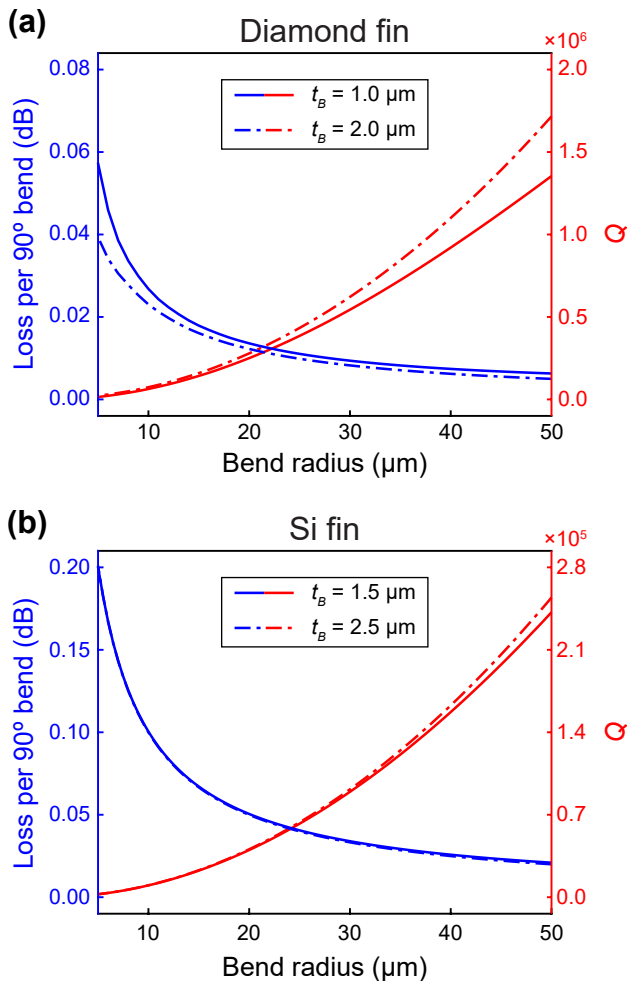


FIG. S4. **Bending loss.** The loss per 90° bend and Q -factor of a ring resonator as a function of bend radius are shown for (a) diamond fin and (b) silicon fin.

The design in Fig. S2 uses Cauchy's equation, $n = A_1 + (\lambda_1/\lambda)^2$, with values of A_1, λ_1 given in table S1 to model the dispersive refractive index of silicon carbide.

TABLE S1. **Sellmeier equation parameters**

Material	i	A_i	λ_i (μm)	Ref.
Diamond	1	0.3306	0.175	[11]
	2	4.3356	0.106	
Si	1	10.6684	0.3015	[4]
	2	0.0030	1.1347	
	3	1.5413	1104	
SiC ^a	1	2.5538	0.1849	[12]
Si ₃ N ₄	1	2.8939	0.13967	[13]
	1	0.6962	0.06840	
	2	0.4079	0.1162	
SiO ₂	2	0.4079	0.1162	[4]
	3	0.8975	9.8962	
	3	0.8975	9.8962	

^a Modeled using Cauchy's equation

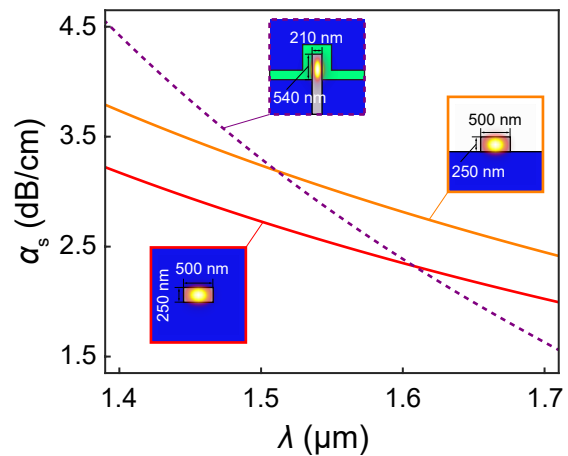


FIG. S5. **Scattering loss.** Propagation loss due to sidewall roughness is compared for a Si fin waveguide and a Si channel waveguide with both air and SiO₂ cladding as a function of wavelength. Sidewall roughness is modeled with a standard deviation of $\sigma_s = 2$ nm and a correlation length of $L_c = 5$ nm.

E. Scattering loss

Scattering loss due to sidewall roughness in a Si fin waveguide and a $500 \text{ nm} \times 250 \text{ nm}$ Si channel waveguide with both air and SiO₂ cladding is modeled using the method given in Ref. [14] with an exponential autocorrelation characterized by a sidewall roughness standard deviation of $\sigma_s = 2$ nm and a correlation length of $L_c = 5$ nm. The lowest order $|0, 0, \hat{x}\rangle$ (quasi-TE) mode has been used for both types of waveguides. The results of this calculation are shown in Fig. S5.

To a first order approximation, the scattering loss coefficient, α_s , is proportional to both the overlap of the mode intensity profile with the waveguide sidewall, as well as the square of the index contrast between the guiding medium (Si in our case) and the cladding (Si₃N₄ for the fin waveguide, SiO₂ or air for the channel waveguide) [14, 15]. While the mode intensity profile overlap with the vertical sidewall is larger for the fin waveguide the index contrast is lower, resulting in marginally higher scattering loss in the fin waveguide at shorter wavelengths and lower loss at higher wavelengths. We note that the waveguides shown in Fig. S5 do not provide an exhaustive comparison between the two types of waveguides; however, they do illustrate that the fin waveguide geometry does not exhibit a substantial difference in propagation loss due to sidewall scattering as compared to a standard channel waveguide.

F. Group velocity dispersion

The waveguide dispersion parameter, which encompasses effects of both waveguide and material dispersion, is defined as [3]:

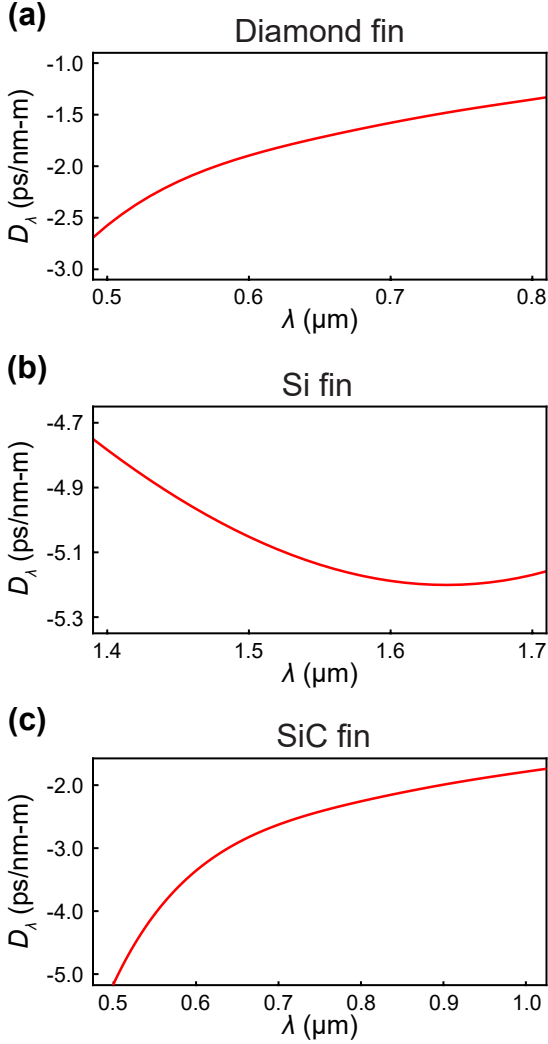


FIG. S6. **Group velocity dispersion (GVD)**. GVD parameter as a function of wavelength for the **a** diamond, **b** silicon, and **c** silicon carbide fin waveguides in Fig. 4a,b of the main text, and Fig. S2.

$$D_\lambda = -\frac{1}{c\lambda} \left(\lambda^2 \frac{d^2 n_{\text{eff}}}{d\lambda^2} \right) \quad (\text{S.34})$$

and has been plotted in Fig. S6 for the waveguides shown in Fig. 4 of the main text and Fig. S2.

TABLE S2. **Anisotropic etches of high-refractive index materials**

Material	Chemistry	Aspect ratio	Ref.
Si	F or Cl_2 -based	> 50 : 1	[16]
InP	$\text{Cl}_2/\text{N}_2/\text{Ar}$	> 8 : 1	[17]
Diamond	O_2	> 10 : 1	[18]
SiC	SF_6/O_2	> 7 : 1	[19]

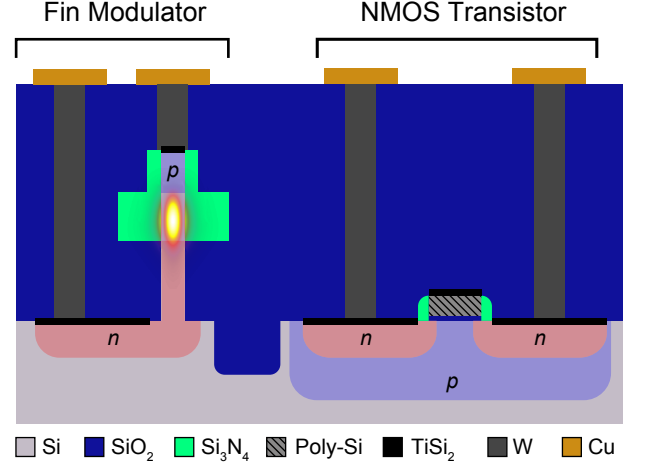


FIG. S7. **CMOS implementation**. Schematic of a fin waveguide modulator co-integrated with an NMOS transistor. Devices are not to scale.

G. Fabrication feasibility

A potential fabrication flow for the fin waveguide is shown in Fig. 4c of the main text. Candidate processes for each of the fabrication steps in Fig. 4c are as follows:

- Lithography**: Electron beam [20] or deep-UV lithography [20, 21] are suitable for achieving the required waveguide dimensions.
- Anisotropic etch**: Inductively-coupled plasma reactive-ion etches (ICP-RIE) have been developed that provide high-aspect ratio structures in many high-refractive-index materials. Example etches for a few of the materials discussed here are outlined in Table 2 F.
- Low index growth**: Optical quality SiO_2 can be grown by plasma-enhanced chemical vapor deposition (PECVD) or low-pressure chemical vapor deposition (LPCVD) [20, 21]. Alternatively, spin casting can be used for the application of flowable oxides, other low index polymer layers [22], or chalcogenide glasses [23].
- Planarization**: Planarization of the low-index layer can be achieved by chemical-mechanical polishing (CMP) or local oxide growth and anisotropic etching [20, 21].
- Low index etch**: Anisotropic etching of the low index layer can be performed using ICP-RIE or capacitively-coupled RIE [20, 21].
- High index growth**: The high-index confinement layer can be grown by PECVD or LPCVD of Si_3N_4 ($n \approx 2.0$), sputtering of Al_2O_3 ($n \approx 1.8$) or AlN ($n \approx 2.2$), spin casting other high index polymer

layers such as SU-8 ($n \approx 1.5$), or deposition of Hydex ($n = 1.5$ to 1.9) [24].

Each step of the fabrication flow is compatible with a conventional CMOS process used for VLSI electronics [20, 21], making the fin waveguide a candidate for

photonic-electronic co-integration. The proposed implementation alleviates the need for silicon-on-insulator (SOI) with a thick buried-oxide-layer, providing a pathway for implementing optical interconnects on VLSI chips. A schematic of a fin waveguide co-integrated with an NMOS transistor is shown in Fig. S7.

-
- [1] A. B. Fallahkhair, K. S. Li, and T. E. Murphy, *IEEE J. Lightwave Technol.* **26**, 1423 (2008).
- [2] H. Nishihara, M. Haruna, and T. Suhara, *Optical integrated circuits* (McGraw-Hill Book Company, New York, 1989).
- [3] A. Yariv and P. Yeh, *Photonics: optical electronics in modern communications*, 6th ed. (Oxford Univ. Press, NY, 2007).
- [4] B. E. Saleh and M. C. Teich, *Fundamentals of photonics*, 2nd ed., Vol. 22 (John Wiley & Sons, NY, 2007).
- [5] J. D. Joannopoulos, S. G. Johnson, J. N. Winn, and R. D. Meade, *Photonic crystals: molding the flow of light* (Princeton university press, 2011).
- [6] R. R. Grote, *Nanophotonics for Optoelectronic Devices: Extrinsic Silicon Photonic Receivers and Organic Photovoltaics*, dissertation, Columbia University in the city of New York (2014).
- [7] P.-R. Loh, A. F. Oskooi, M. Ibanescu, M. Skorobogatiy, and S. G. Johnson, *Phys. Rev. E* **79**, 065601 (2009).
- [8] J. B. Driscoll, X. Liu, S. Yasserli, I. Hsieh, J. I. Dadap, and R. M. Osgood, *Opt. Express* **17**, 2797 (2009).
- [9] J. Cardenas, M. Yu, Y. Okawachi, C. B. Poitras, R. K. Lau, A. Dutt, A. L. Gaeta, and M. Lipson, *Opt. Lett.* **40**, 4138 (2015).
- [10] W. W. Lui, C.-L. Xu, T. Hirono, K. Yokoyama, and W.-P. Huang, *IEEE J. Lightwave Technol.* **16**, 910 (1998).
- [11] R. Mildren and J. Rabeau, *Optical engineering of diamond* (John Wiley & Sons, 2013).
- [12] P. T. Shaffer, *Appl. Opt.* **10**, 1034 (1971).
- [13] T. Bååk, *Appl. Opt.* **21**, 1069 (1982).
- [14] F. Grillot, L. Vivien, S. Laval, and E. Cassan, *IEEE J. Lightwave Technol.* **24**, 891 (2006).
- [15] F. Payne and J. Lacey, *Optical and Quantum Electronics* **26**, 977 (1994).
- [16] B. Wu, A. Kumar, and S. Pamarthy, *J. Appl. Phys.* **108**, 051101 (2010).
- [17] S. Park, S.-S. Kim, L. Wang, and S.-T. Ho, *IEEE J. Quantum Electron.* **41**, 351 (2005).
- [18] B. J. Hausmann, M. Khan, Y. Zhang, T. M. Babinec, K. Martinick, M. McCutcheon, P. R. Hemmer, and M. Lončar, *Diamond and Related Materials* **19**, 621 (2010).
- [19] J. Choi, L. Latu-Romain, E. Bano, F. Dhalluin, T. Chevolleau, and T. Baron, *Journal of Physics D: Applied Physics* **45**, 235204 (2012).
- [20] J. D. Plummer, M. Deal, and P. B. Griffin, *Silicon VLSI technology: fundamentals, practice, and modeling* (Prentice Hall, NJ, 2000).
- [21] S. Wolf, *Microchip manufacturing* (Lattice press, CA, 2004).
- [22] J. Halldorsson, N. B. Arnfinnsdottir, A. B. Jonsdottir, B. Agnarsson, and K. Leosson, *Opt. Express* **18**, 16217 (2010).
- [23] B. J. Eggleton, B. Luther-Davies, and K. Richardson, *Nature Photon.* **5**, 141 (2011).
- [24] D. J. Moss, R. Morandotti, A. L. Gaeta, and M. Lipson, *Nature Photon.* **7**, 597 (2013).